Seismic velocity anomalies beneath SE Brazil from *P* and *S* wave travel time inversions

M. Schimmel[1] and M. Assumpção
Department of Geophysics, University of São Paulo, São Paulo, Brazil

J. C. VanDecar
Carnegie Institution of Washington, Washington, D.C., USA

Received 28 December 1999; revised 22 May 2002; accepted 21 October 2002; published 10 April 2003.

[1] We present the result from teleseismic travel time inversions for *P* and *S* wave data mainly recorded at portable broadband stations in SE Brazil. The stations were deployed at 45 sites within an area 1000 × 1700 km during the years 1992–1999. More than 10,000 relative *P* and *S* wave arrival times, including core phases, were obtained from the waveforms using a new coherence functional. These *P* and *S* relative phase times are independently inverted for slowness perturbations, earthquake relocations, and station corrections. The final models represent the least amount of structure required to explain the residuals within a defined standard error. The robust and consistent features in the velocity anomaly models are interpreted and their resolution is tested with synthetic case inversions. We confirm the existence of a cylindrical low-velocity anomaly beneath the Paraná basin, which has been interpreted by *VanDecar et al.* [1995] as the fossil conduit through which the initial Tristan da Cunha plume head traveled to generate the Paraná–Etendeka flood basalts about 130 Ma. We now show that this low-velocity cylindrical structure seems to be confined to the upper mantle. Beneath the upper mantle, the velocity anomalies show a N-S oriented pattern, which we interpret as due to the Nazca plate subducted slab. At lithospheric depths, the Archean, southern part of the São Francisco craton, shows high velocities down to 200–300 km. All areas with Late Cretaceous postrift alkaline intrusions are characterized by low velocities at lithospheric depths. *INDEX TERMS:* 7218 Seismology: Lithosphere and upper mantle; 8180 Tectonophysics: Tomography; 9360 Information Related to Geographic Region: South America; *KEYWORDS:* seismic regional tomography, SE Brazil, Paranã-Etendeka flood basalts, Tristan da Cunha plume, subducted Nazca plate, alkaline intrusions

Citation: Schimmel, M., M. Assumpção, and J. C. VanDecar, Seismic velocity anomalies beneath SE Brazil from *P* and *S* wave travel time inversions, *J. Geophys. Res.*, *108*(B4), 2191, doi:10.1029/2001JB000187, 2003.

1. Introduction and Motivation

[2] The study of the Brazilian upper mantle structure is important for the determination of tectonic regimes, the thermal and geological evolution of the South American continent, and to understand the regional convection style and forces. This study at scales of cratons and fold belts is motivated by the presence of the major structural units of western Gondwana, younger mobile fold belts and relics of the opening of the South Atlantic ocean such as continental flood basalts (CFB) and dyke swarms. The upper mantle structure is expected to correlate to these surface tectonic environments and can reveal hidden anomalies and limits of structural units, which are controversial due to the presence of cover rocks.

[3] A prime tool to illuminate mantle structure is seismic tomography. Although it lacks the resolving power to constrain mantle discontinuities, it provides us with reconstructions of the long and intermediate scale structure. We use this tool to map the *P* and *S* wave velocity anomalies underneath SE Brazil. The data set used consists of relative *P* and *S* wave arrival times from teleseismic events. These relative times are inverted for slowness perturbations within the target volume, for earthquake relocations, and station corrections. The inversion procedure follows the approach described by *VanDecar et al.* [1995], which has been successfully applied by *Wolfe et al.* [1997] and *Ritsema et al.* [1998], among others.

[4] In essence, the geology of our study area has been formed by several fragmentations and collisions during the Pan-Africa or Brasiliano orogeny [*Brito Neves and Cordani*, 1991; *Trompette*, 1994] which lasted until 540 Ma and resulted in the consolidation of the Gondwana supercontinent. Gondwana consisted of several fold belts of Proterozoic terranes partly subducted and cratons of varying ages

[1]Now at Institute of Earth Sciences "Jaume Almera," Consejo Superior de Investigaciones Cientificas (CSIC), Barcelona, Spain.

Copyright 2003 by the American Geophysical Union.
0148-0227/03/2001JB000187$09.00

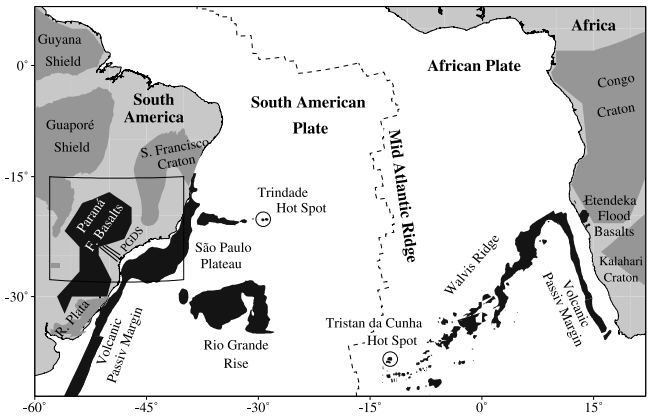

Figure 1. Schematic map displaying the major cratons and the key structural elements of the opening of the South Atlantic (130 Ma to present) correlated with the Tristan da Cunha hot spot. The cratons are tectonic units from western Gondwana and are of Archean and lower Proterozoic age. Their exact boundaries often remain unclear.

but mostly with Archean nuclei. Subsequent to assembly, mostly epeirogenic readjustments and local folding occurred until the opening of the South Atlantic ocean (early Cretaceous) along ancient orogenic belts [*Vauchez et al.*, 1997]. At latitudes ~30°S the opening is related to the Tristan da Cunha hot spot which likely caused via decompressional melting and/or passive heating huge lava flows (~130 Ma) exposed as CFB in southeastern South America (Paraná Basin) and southwestern Africa (Etendeka). The exact role of the Tristan hot spot is still controversial [e.g., *O'Connor and Dunkan*, 1990; *Peate et al.*, 1999]. The key tectonic elements of South America and the conjugate African margin are displayed in the schematic map from Figure 1, which also shows the link of the Paraná and Etendeka flood basalts via the Rio Grande Rise and Walvis ridge to the present Tristan da Cunha hot spot, located east of the South Atlantic ridge. In Figure 1 PGDS stands for Ponta Grossa dike swarm and is often referred to as the system through which the Paraná CFB were fed [*Renne et al.*, 1996].

[5] A previous tomography study by *VanDecar et al.* [1995] revealed a low-velocity cylindrical structure in the upper mantle underneath the Paraná Basin. *VanDecar et al.* [1995] interpreted the cylindrical structure as the fossil conduit through which the initial Tristan da Cunha plume head traveled to generate the Paraná–Etendeka CFB. If the velocity anomaly is assumed to arise from a thermal perturbation, it would correspond to a temperature increase of about 200°C [*VanDecar et al.*, 1995]. This structure currently lies beneath the Paraná basin, indicating that the underlying upper mantle has been in coupled motion with the overlying plate since the opening of the South Atlantic Ocean. Recent fundamental mode surface wave tomography studies by *Silveira et al.* [1998] and *Vdovin et al.* [1999] did not have resolution to identify the low-velocity conduit. The conduit, however, was detected by the surface wave tomography study, including higher modes, by *Van der Lee et al.* [2001], which used several stations in SE Brazil. The use of higher modes and the additional stations permitted a better lateral and depth resolution than the previous surface wave studies. Besides the low-velocity anomaly beneath the Paraná basin other cylindrical low-velocity anomalies have also been observed beneath other flood basalt provinces such as the Deccan traps in NW India [*Kennett and Widiyantoro*, 1999] and the Ontong-Java Plateau [*Richardson et al.*, 2000]. If these anomalies are related to the flood basalt generation then the persistence beneath these areas implies that these anomalies moved with the corresponding plates.

[6] In SE Brazil we increased the aperture of the seismic network, the number of stations, and the data collection period to image an enlarged volume, and to obtain a more detailed separation of geological structures such as the São Francisco craton and an extension of the study to greater depth. Most of our study area, parts of the Paraná Basin, Brasilia Belt, Ribeira Belt, and São Francisco craton, had not been imaged before at regional scales. The new *P* and *S* wave velocity anomaly models are obtained from individual inversions and consistently show the gross structure, which for shallow depth, often correlates with the surface geology. Inversions for subsidiary data sets, different parameters, and study volumes show the robust features that are interpreted with help of synthetic test inversions. This study shows the first reconstructions from the base of the cylindrical low-velocity anomaly, which is important for its interpretation and the characterization of the coupling between upper and lower mantle beneath SE Brazil. Further, the south São Francisco craton is imaged with roots down to 200 km depth. In the surrounding belt systems, we find shallow low-velocity anomalies that correlate with Late Cretaceous alkaline intrusions at the Earth surface. Below the base of the upper mantle, parts of the subducted Nazca plate are indicated.

2. Stations, Event Selection, and Data Processing

2.1. The Seismic Station Network

[7] The database is constructed from seismic waveforms recorded at stations deployed at more than 45 sites within an area of about 1000 × 1700 km during the years 1992–1999. Up to 15 stations were in operation at any time. Almost all stations were equipped with three-component broadband seismometers. Most stations were from a joint project (Brazilian Lithosphere Seismic Project 1992 (BLSP92)) of the Carnegie Institution of Washington and the University of São Paulo (USP) and from a continuation of this project by the USP (BLSP95). Figure 2 shows a map with the station locations used to create the relative *P* and *S* wave travel time database. The BLSP broadband stations are indicated by triangles. The squares (Figure 2) mark two Global Telemetered Seismic Network (GTSN) stations located in Brasilia and Villa Florida (Paraguay), one Geoscope station, and four temporary stations from the University of Brasilia (UnB). In addition we used data from short period sensors (circles in Figure 2) to increment the *P* wave data set. The short period data belong to the Seismic Network of the USP (RESUSP) and the BLSP95 project. All stations have been equipped with GPS receiver to provide accurate station location and time. We corrected the time of all traces recorded by the portable stations and discarded data whenever a GPS failure could not guarantee accurate time.

2.2. The Event Selection

[8] We selected *P* and *S* phases from events at angular distances between 30° and 95° with body wave magnitude

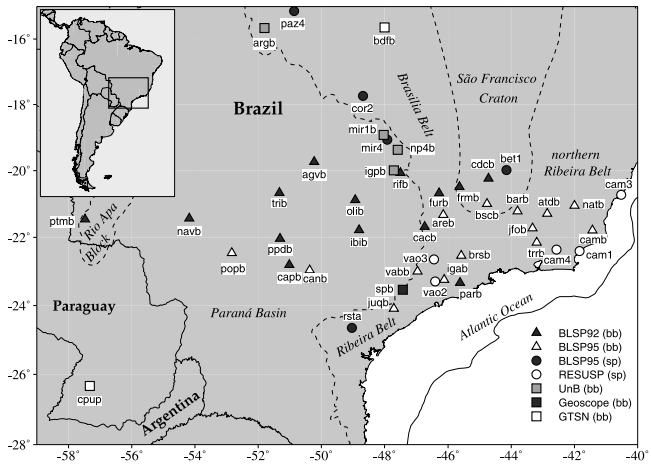

Figure 2. Map with the sites of seismic stations used for the relative arrival time data set and gross geological provinces. The solid lines are political boundaries and the dashed lines denote the main geological provinces. Up to 15 stations have been in operation at any time to record the events from 1992 to 1999. The stations are sorted by projects or owner. "bb" and "sp" stand for broadband and short-period sensor, respectively. The short-period stations are used to increment the *P* wave data set.

(m_b) larger than 4.6. The USGS PDE database provided the hypocenters. For the selected distance range, the *P* and *S* waves turn in the lower mantle which means that we avoid difficulties with the upper mantle triplications and the nonlinearity of the ray path which otherwise turns where the heterogeneities are strongest. In addition, we picked events ($m_b \geq 5.4$) that permit an unambiguous detection of the core phases *PKPdf*, *ScS*, *SKSac*, and *SKKSac* by their slowness and travel time. *PKPdf*, *SKSac*, and *SKKSac* waves propagate through the core to the stations along steep paths. Also, the core reflected *ScS* waves are steeply incident on the area below the stations.

2.3. The Relative Travel Time Picking

[9] Our observations are relative arrival times of *P* and *S* waves simultaneously recorded at four or more stations. The data which we use in the inversions are relative residuals (the mean travel time residual per event has been removed) to decrease the possible biases from outside the target volume. A "multichannel cross correlation" (MCCC) technique by *VanDecar and Crosson* [1990] which exploits the waveform coherence over the network has been adapted for the determination of relative arrival times. This MCCC technique uses all possible pairs of waveforms and solves in the least squares sense for the best set of relative arrival times for all stations. We incorporated a new cross-correlation function [*Schimmel*, 1999] into the MCCC technique and call this modified derivative MCPCC, which stands for "multichannel phase cross correlation." The backbone of the phase cross correlation (PCC) is the instantaneous phase of the analytic traces. PCC determines waveform similarity by the greatest number of coherent samples rather than the largest sum of cross products. Therefore, it is not biased by the large amplitude portions in the correlation window.

[10] Figure 3 shows an example of the picking procedure using an event at the North Atlantic ridge (6 October 1996, 13.23°N, 44.97°W, 10 km depth, m_b = 5.1). The epicentral distance to station spb is 36.7°. Figure 3a shows the unfiltered vertical recordings from five broadband stations. The seismograms have been aligned with respect to their theoretical *P* wave arrival time, estimated for the global reference model IASP91 [*Kennett and Engdahl*, 1991]. Note that the identification of the *P* phases requires the use of appropriate filtering of the data. Figure 3b shows the data after band passing (0.8–1.6 Hz) and application of the MCPCC technique to determine the relative arrival times. The data are now aligned with respect to their relative times. Although we do not know the exact onset time, it is observed that the theoretical arrival is about 3 s faster in this example. A 2.2 s difference is due to the use of the IASP91 model rather than the Jeffreys-Bullen travel time tables, which are employed by the USGS to obtain the PDE hypocenter. The remaining 1 s difference could be due to an event mislocation of about 10 km or structure, which affects the travel time to all stations. These uncertainties are removed by using the relative residuals as data. Other effects of using relative residuals will be discussed later.

[11] In Figure 3c, seismograms are plotted on top of each other to demonstrate the correctness and quality of their alignment. We use only arrivals that are coherently seen over the array. Data and correlation settings, such as frequencies and window length and position, are hand selected and the cross-correlation iterations start at low frequencies to avoid cycle skipping and phase misinterpretation. The final correlation is performed on a broad high-frequency band to determine the stationary group time of the first signal or portion of signal. The uncertainties of the measurements depend on the data quality. With data comparable to the records from Figure 3 the standard deviations of the time measures for different window length and filter settings are about 20 ms or less. With bad data and similar variations in the cross-correlation settings we

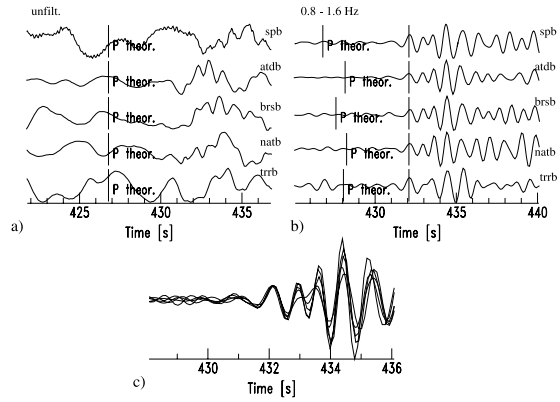

Figure 3. (a) Unfiltered vertical component broadband recordings for an event at the North Mid-Atlantic Ridge. The traces are aligned with respect to their theoretical *P* wave arrival time. The time axis corresponds to the top trace from station spb. (b) Same as (a), but the data have been band passed (0.8–1.6 Hz) and aligned with respect to their relative arrival times. (c) The recordings from (b) are overlaid to show signal coherence.

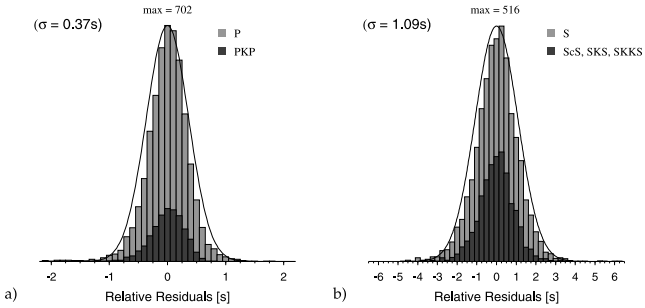

Figure 4. Histograms for the relative *P* wave (a) and *S* wave (b) residuals after correction of station elevation. Core phases and first arrivals are separated by gray tones. A Gauss function with corresponding standard deviation and maximum count has been added for reference.

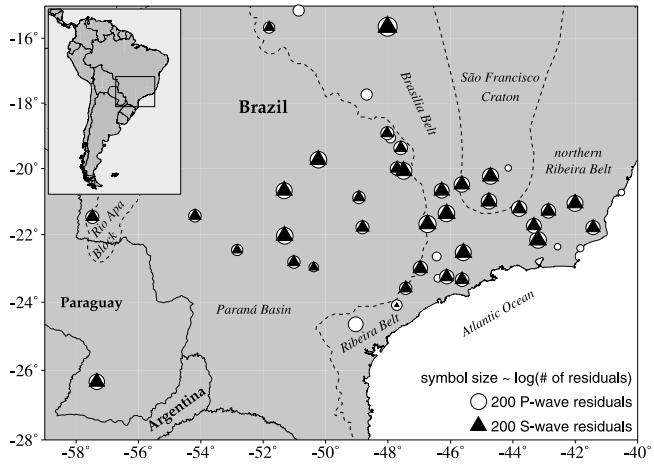

Figure 5. Distribution of the *P* wave (circles) and *S* wave (triangles) arrival totals as function of station site. The symbol size is proportional to the base-10 logarithm of the number of arrivals.

obtain uncertainties of about 80 ms. The overall data uncertainty is larger owing to other error sources such as arrival misinterpretations.

[12] The waveforms of the short period instruments have been transformed to mimic broadband records and used together with the vertical broadband data at frequency bands around 1 Hz. The picking is performed at a high-frequency band since a high-frequency approximation of wave propagation (ray theory) is applied in the inversion procedure. The most common frequencies used for the *P* arrivals range between 0.8 and 2.5 Hz. The corresponding seismic wavelengths in the upper mantle are smaller than 12 km.

[13] The *S* and *ScS* phases are identified on the transverse components to minimize the contamination of the *S* arrivals by *P* or *P*-to-*S* converted waves. Nevertheless, the identification of the *S* phases is more difficult than for the *P* phases due to their larger intrinsic attenuation, the larger noise on the horizontal components, and presence of scattered *P* and *SV* waves that contaminate the transverse components. Therefore, we are restricted to low frequencies. The lowest-frequency band used is from 0.05 Hz to 0.1 Hz with corresponding wavelength of about 60 km. Generally higher-frequency bands could be applied which decreased the seismic wavelength to 40 km or less.

2.4. The Final Data Sets

[14] We determined the relative arrival times for 4281 *P* (656 events), 1086 *PKP* (152 events), 2889 *S* (464 events), 456 *ScS* (73 events), 554 *SKS* (89 events), and 864 *SKKS* arrivals (138 events). The travel times were corrected for station elevations using the theoretical ray incidence and averaged *P* wave and *S* velocities of 5.8 and 3.5 km/s. The relative *P* and *S* wave residual distributions of the final data sets are shown in Figure 4. The standard deviations for the *P* and *S* wave data are 0.37 and 1.09 s, respectively. The distributions for the core phases and first arrivals are illustrated in black and gray, respectively. It can be seen from the comparison with the corresponding Gauss function (solid line) that the data distribution deviates slightly from a Gaussian distribution at the larger residuals, especially for *P* waves. The data distribution is important for the choice of the inversion procedure. For instance, large outliers are given relatively more weight in a least squares inversions which may result in spurious anomalies. The data distribution as function of station site is depicted in Figure 5. The symbol sizes, circles for *P* waves and triangles for *S* waves, are proportional to the base-10 logarithm of the number of arrivals. The unequal data distribution is due to varying deployment times of each station. Figure 6 shows the relative travel time residuals of the direct *P* and *S* phases as function of back azimuth at 6 distinct stations, for all

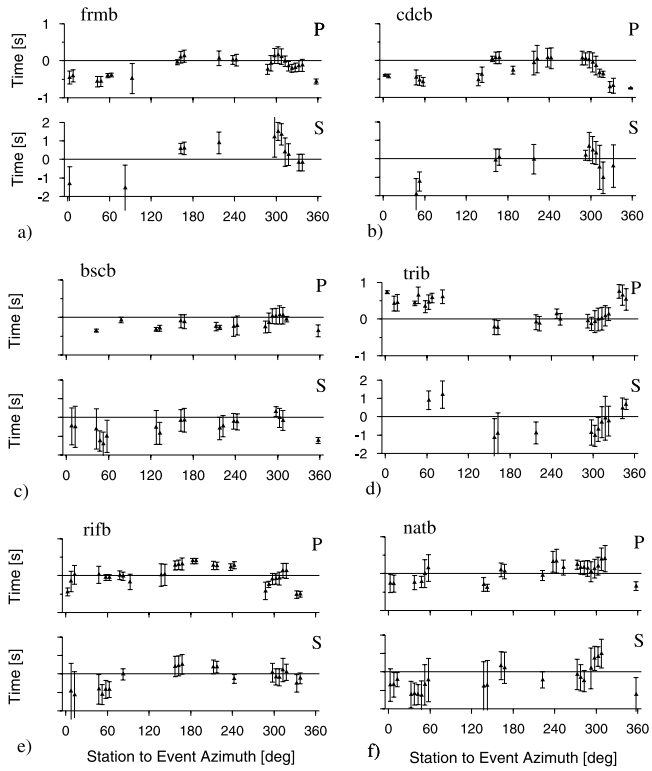

Figure 6. Relative travel time residuals of the direct *P* and *S* phases as functions of back azimuth at stations *FRMB* (a), *CDCB* (b), *BSCB* (c), *TRIB* (d), *RIFB* (e), and *NATB* (f). The symbols and error bars mark the means and standard deviations of at least four measures within 10° bins centered every 5°.

distances between 30° and 95°. Each symbol and error bar mark the mean and standard deviation of at least 4 measurements within a 10° bin centered at every 5°. The events often cluster at certain distance ranges due to their distribution mainly along the plate boundaries. The standard deviation is not a quality measure, but indicates variation of the data in each bin mainly due to different epicenter distances. From Figure 6a, correlation of the relative *P* and *S* wave residuals is observed at each station. This is expected for structure that affects the *P* and *S* waves in a correlated manner. The stations shown in Figures 6a–6c are located in the São Francisco craton. Their relative residuals roughly follow the same trends, for instance fast arrivals at back azimuths between 320° and 120° and could be inherent to the same long scale structure. The similar pattern for the nearby stations in the São Francisco craton, and the observed correlation of *P* and *S* wave residuals show that the data carry consistent informations on velocity structure.

[15] Figure 7 shows the ray incidence angles at the depth of 400 km as function of back azimuth and the root-mean-square (RMS) data residual as function of incidence angle. Every symbol plotted in Figures 7a and 7b corresponds to a ray in our *P* and *S* wave data set, respectively. The band-shaped distribution of the ray incidence angles is due to the selected distance ranges. The overall patchiness is caused by the unequal distribution of earthquakes over the globe. The large distribution of angles guarantees that the ray paths cross at high angles, which is necessary for the isolation of anomalies in the travel time inversion. The resolution is a function of the ray distribution. The RMS data residual as a function of incidence angle (solid lines in Figure 7) was calculated using a moving box-car window of 2° width centered at every integer degree value. The slightly smaller RMS values for the core phases can partly be attributed to the steeper ray path and smaller travel time in the more heterogeneous upper mantle, and to more rigorous data selection criteria. The coarse and fine dashed lines in Figure 7 show the distribution after the first and final iteration of the linear inversion.

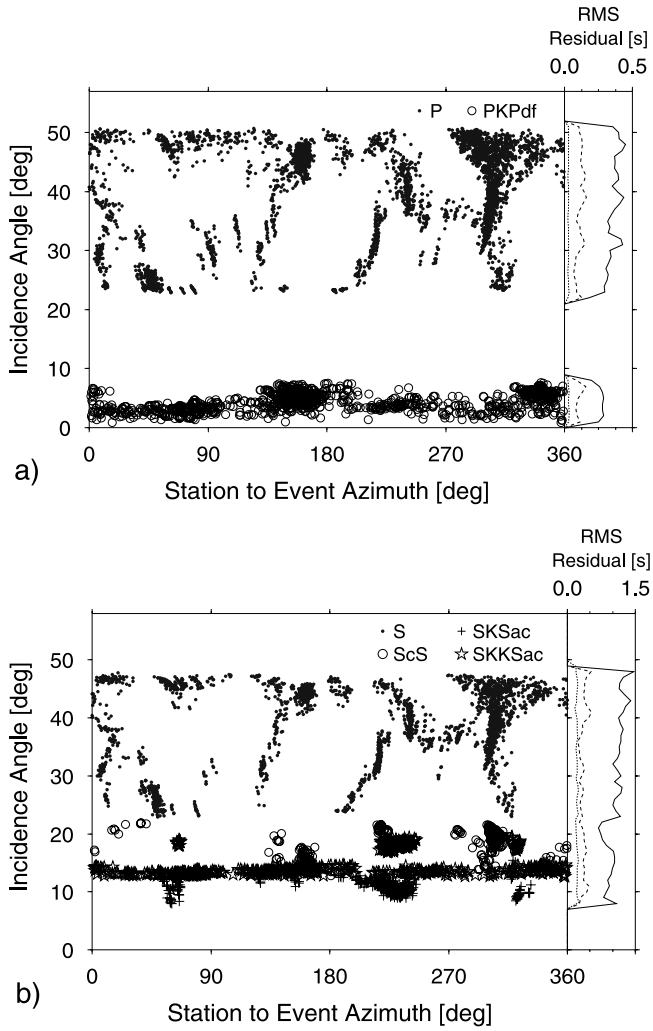

Figure 7. Distribution of ray incidence angles at 400 km depth as function of back azimuths and RMS residuals for the *P* wave (a) and *S* wave (b) data set. Every symbol corresponds to a ray. The horizontal band-shaped occurrence of incidence angles is due to the selected distance ranges. The data points cluster due to the uneven distribution of events. The RMS residuals of the data sets (solid lines) and after the first (dashed lines) and final (dotted lines) inversion iteration are calculated within a moving 2° window.

3. The Travel Time Inversion

[16] The inversion follows the approach described by *VanDecar et al.* [1995]. In the following we briefly point out the important aspects and show the obtained results.

3.1. The Model Parameterization

[17] The model perturbations beneath the stations are parameterized by splines under tension [*Cline*, 1981; *Neele et al.*, 1993] which are pinned at a series of regular knots. This interpolation scheme allows for a smooth slowness distribution and accurate ray tracing. The volume considered extends from −31° to −11° in latitude, −63° to −36° in longitude, and to 1600 km in depth. A fine grid with $\frac{1}{3}^\circ$ horizontal and 33 km depth node spacing is defined for latitudes between −28° and −14°, longitudes between −60° and −39°, and down to a depth of 700 km. Outside this volume the node spacing is initially increased to 0.5° horizontally and 50 km in depth; near the outer border the spacing is 1° horizontally and 100 km in depth. A total of 89,280 nodes are used to parameterize the slowness perturbations. The choice of the grid spacing is a function of wavelength, the amount of data and data distribution. The grid spacing in the better resolved volume was chosen to detect structures with minimum scale length of about 60 km compatible with the upper bound of the *S* wavelength. Whether structures with minimum scale length can be mapped, however, depends on the ray coverage that is highly variable as shown in Figure 8. The fine grid spacing results in an overparameterization, which in the inversion is compensated with smoothness constraints.

3.2. The Assumptions

[18] It is expected that the seismic energy travels on a ray path to the station. The problem has been linearized based on the assumption of weak perturbations. This means it is expected that the true rays and earthquake locations are

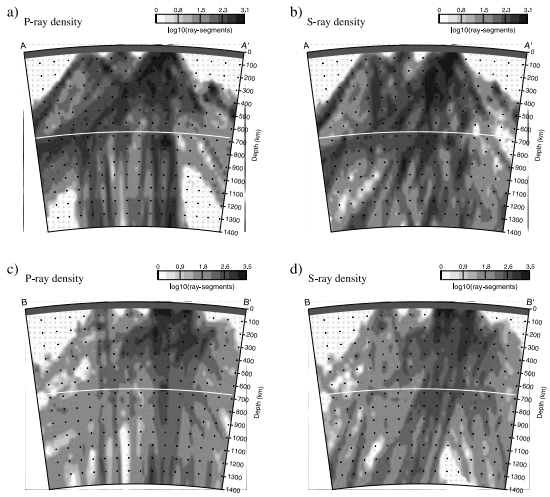

Figure 8. Distribution of length sum of ray segments that constrain the *P* wave (a and c) and *S* wave (b and d) velocity perturbations along the cross sections A-A′ and B-B′, respectively, from Figure 11.

linearly close to the initial guess. Further, it is assumed that data bias from structure outside the target volume is negligible given our use of relative residuals, i.e., removing the mean residual from the data for a given event, or absorbed by the station terms and low-resolution areas.

3.3. The Inversion

[19] The *P* and *S* wave relative phase times are independently inverted. Earthquake relocations and station corrections are simultaneously inverted with the model perturbations. With earthquake relocation, we mean that we permit small adjustments of the hypocenter in space. The relative residual times do not permit an earthquake relocation in time. The small relocation acts as additional buffer to absorb data inconsistencies caused by event mislocations. Similarly, the station terms are introduced to absorb systematic time contributions caused by local shallow heterogeneities beneath the individual stations. The linear problem of finding the model perturbations is partly underdetermined (ill-posed) which means that the inversion is nonunique. Occam's razor [*Constable et al.*, 1987] is followed to search for the model with the least amount of structure to explain the relative time residuals within a defined standard error. Because of noise in the data, one should not try to make the misfit function as small as possible, which would likely map noise into structure. To constrain the inversion to the least amount of structure the regularization term contains the linear combination of the first-order and second-order derivative operators onto the model perturbations. As consequence, the inversion results are smooth and contain the minimum structure that can be considered the probable lower bound of the true anomalies in the resolved areas.

[20] Numerically, the conjugate gradient method LSQR [*Paige and Saunders*, 1982] is employed for the inversion. Several inversions are iteratively performed. Except for the first iteration, equations for residuals larger than 1.5 standard deviation are systematically downweighted [*Huber*, 1981]. This approach leads to a robust solution with L2 residual minimization for data within 1.5 residual standard deviations and L1 minimization of the equations with larger residuals. It accounts for the more suitable double exponential distribution of the larger residuals and decreases the influence of gross outliers among the measurements [e.g., *Pulliam et al.*, 1993]. As a consequence, the final model does not contain the structure roughness that otherwise might have been introduced by a few outliers from possibly noisy measurements. Several inversions on subsidiary data sets and with varying regularization parameters were computed and the results compared to reveal the robust features of our tomographic reconstructions. The subsidiary data sets were obtained by omitting systematically the data of individual stations or station groups (e.g., short period data) or by randomly omitting part of the measurements. The reconstructions based on these subsidiary data sets are surprisingly robust. Differences are only observed for details that we will not interpret.

3.4. The Results

[21] The Figures 9–11 show the results obtained with the inversion procedure described above. The warm and cold colors mark slower and faster than average velocities for that depth. Areas with ray density less than 20 rays/(100 km)^3 are darkened in the images. Figures 9 and 10 show horizontal cross sections of the *P* and *S* wave velocity anomalies, respectively, at different depths. In these images the squares mark the station locations used in the inversions and the white lines mark the locations of the vertical cross sections (A-A′ and B-B′) shown in Figure 11. The yellow circles in Figures 9a and 10a denote locations with Late Cretaceous/early Tertiary alkaline intrusions (90–55 Ma). In Figure 11, we compare the *P* wave (first column) and *S* wave (second column) velocity anomalies along the profiles A-A′ and B-B′. The vertical cross sections (Figure 11) are blackened down to 50 km depth since shallow structures are difficult to resolve owing to the absence of crossing ray paths just underneath the stations. The models explain about 89% of the RMS data residual (from 0.37 to 0.04 s) for *P* waves and 90% of the RMS residual (from 1.09 to 0.104 s) for *S* waves.

[22] The ray density along the cross sections A-A′ and B-B′ is shown in Figure 8. It is obvious from this figure that the structure is differently sampled by our *P* and *S* wave rays which causes some differences in the *P* and *S* wave velocity anomaly models. Besides, small differences in velocity anomaly models can be interpreted as compositional variation, i.e., a varying Poisson ratio can be inferred from the mapped anomalies. Alternatively, the observed differences could be an indication of anisotropy-induced artifacts [*Sobolev et al.*, 1999]. Indeed, upper mantle *S* wave anisotropy has been observed within the study area [*James and Assumpção*, 1996]. Their *SKS* splitting observations are interpreted as due to pure shear deformations. *Sobolev et al.* [1999] show that under these circumstances anisotropy-induced artifacts can be neglected in the isotropic *P* wave travel time inversions. The large variance reductions of our inversions and the consistency between *P* and *S* wave models further suggest that anisotropy-induced artifacts do not govern the results presented.

[23] At shallow depth, a good correlation is obtained between the Late Cretaceous alkaline intrusions (yellow circles in Figures 9a and 10a) and the imaged low-velocity

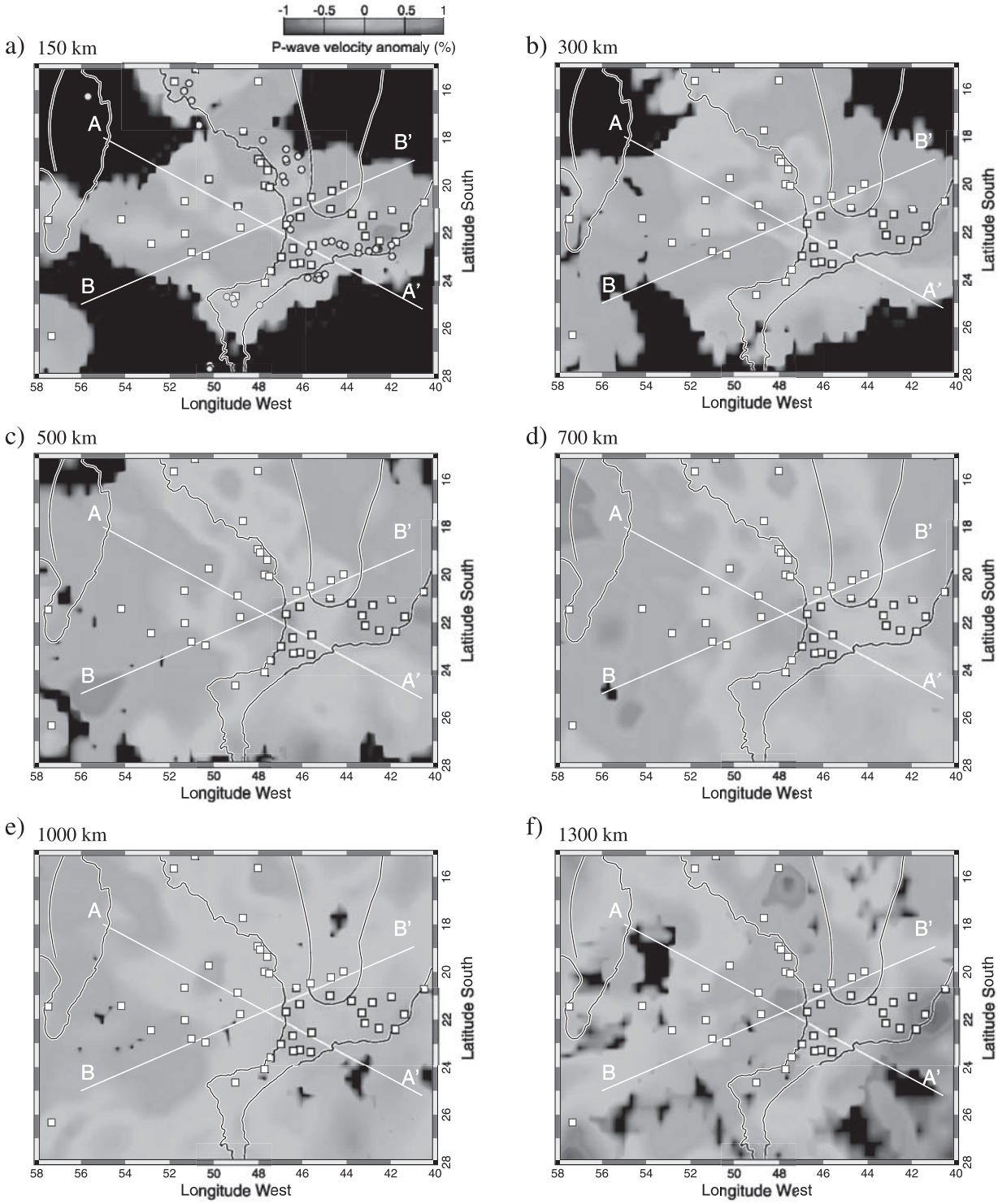

Figure 9. Tomographic reconstructions for the *P* wave phase times at distinct depth levels. White lines mark the intersections with the vertical cross sections (A-A′ and B-B′) displayed in Figure 11. White squares and yellow circles (a) denote station sites and Late Cretaceous alkaline intrusions (ages range from 90 to 55 Ma), respectively. See color version of this figure at back of this issue.

areas in the fold belts. All alkaline provinces occur on top, or at the edges, of lithospheric low-velocity anomalies.

[24] The tomographic *P* and *S* velocity anomaly images consistently show a low-velocity anomaly mainly in the upper mantle in the center of the study volume (Figures 9–11). This structure has been interpreted as the fossil conduit through which the initial Tristan da Cunha plume head traveled to generate the Paraná CFB just before the opening of the South Atlantic Ocean at corresponding latitudes [*VanDecar et al.*, 1995]. It can be seen from the reconstruc-

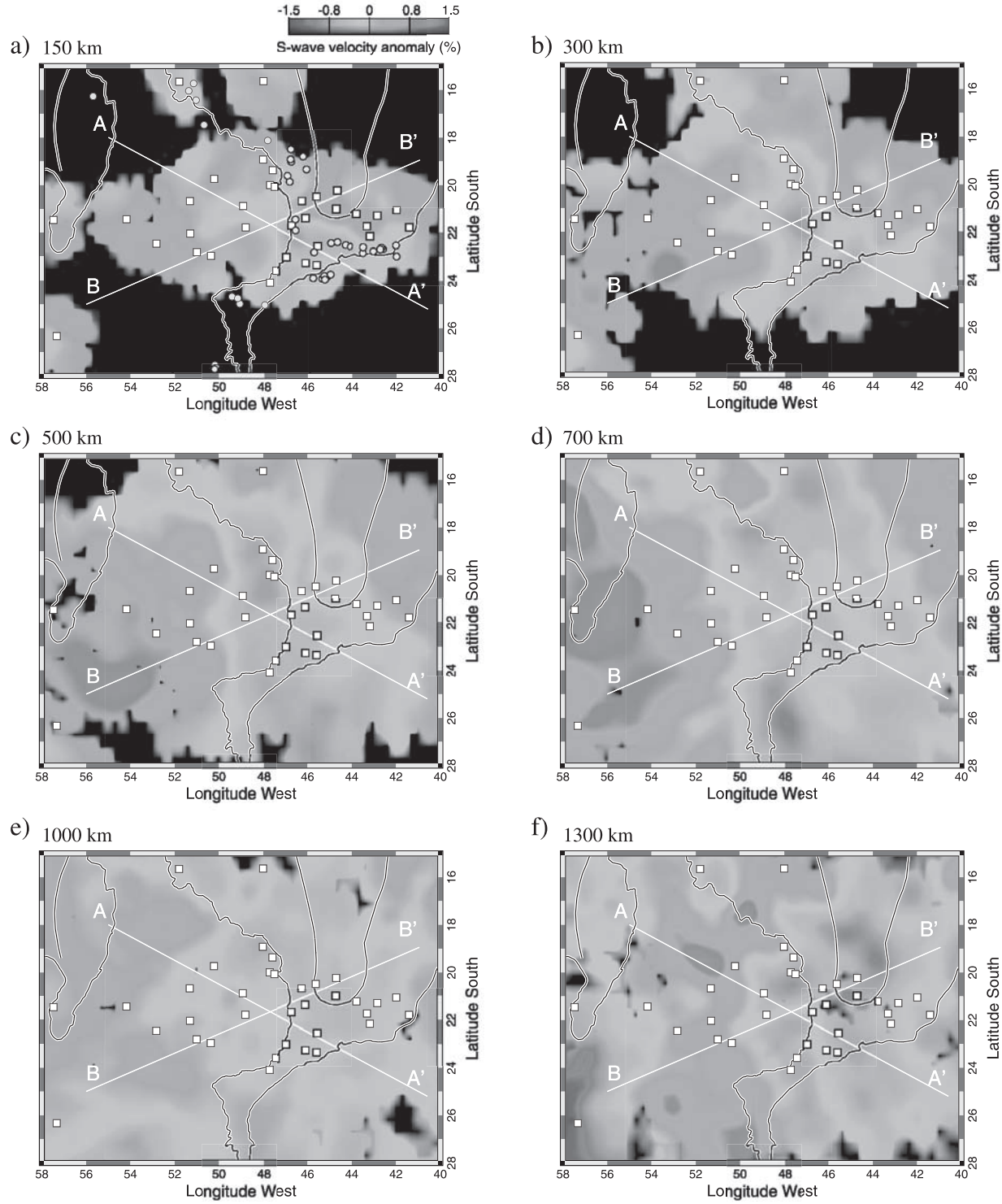

Figure 10. Tomographic reconstructions for the *S* wave phase times at distinct depth levels. White lines mark the intersections with the vertical cross sections (A-A′ and B-B′) that are displayed in Figure 11. White squares denote station sites used in the *S* wave inversion. The yellow circles (a) denote Late Cretaceous alkaline intrusions (ages range from 90 to 55 Ma). See color version of this figure at back of this issue.

tions in Figures 9a–9d and 10a–10d that this low-velocity anomaly increases in volume and elongates into the N-S direction below about 500 km (Figures 9c and 9d and 10c and 10d) down to about 800–900 km (Figure 11). A second low-velocity anomaly is imaged in the lower mantle for the *P* and *S* wave data (Figures 9e and 9f and 10e and 10f) with similar N-S orientation but displaced to the east.

[25] Besides these low-velocity anomalies, distinct fast anomalies are observed. In the *S* and *P* wave images with potentially smaller-scale resolution the São Francisco craton

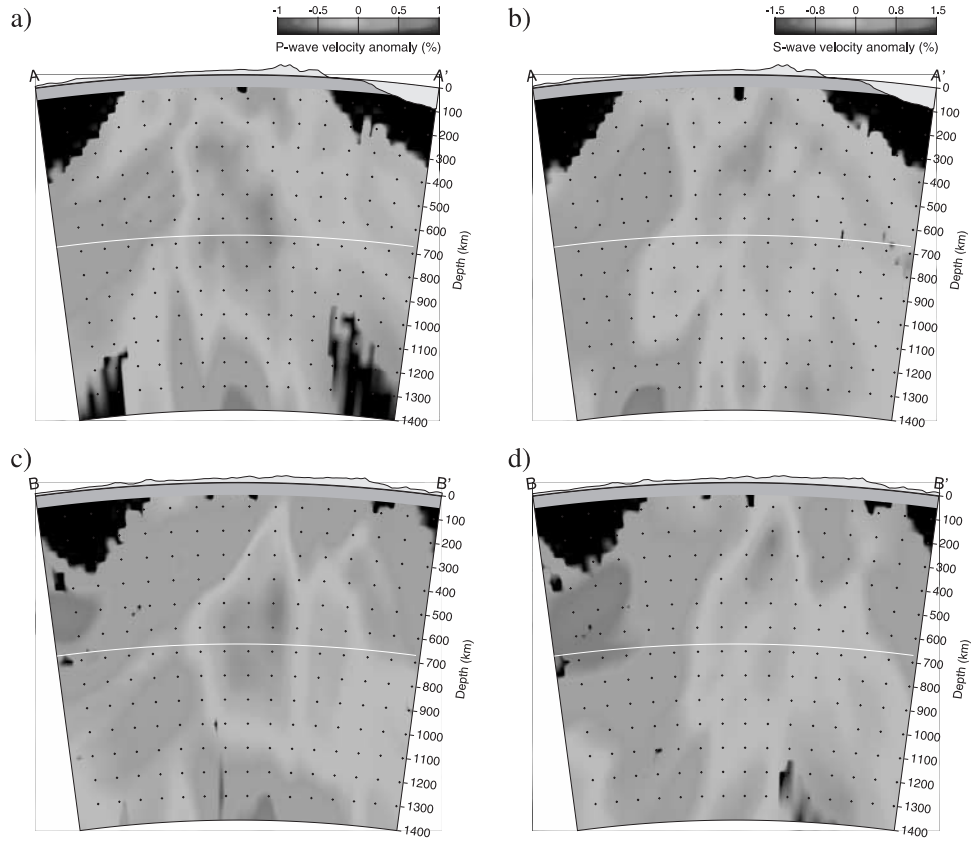

Figure 11. The vertical cross sections A-A′ and B-B′ are displayed for the *P* (left column) and *S* (right column) velocity perturbation models. The elevations at the Earth's surface are multiplied by 30. See color version of this figure at back of this issue.

is visible as a fast-velocity anomaly with roots down to 300 and 200 km, respectively. The small area with shallow fast *P* wave velocities beneath stations *AREB* and *CACB* SW of the craton (Figures 2 and 9a) is a stable feature which appears in the *P* wave models for the different inversion settings. It coincides with the Varginha-Guaxupe complex which consists of granulitic gneisses and migmatites of Archean age, reworked during the Uruaçuano and Brasiliano cycles [*Schobbenhaus*, 1984]. Rocks of the same complex are found in the northern Ribeira belt (SE of the São Francisco craton roughly between stations TRRB and NATB) which coincides with a fast anomaly in Figures 9a and 9b. The high velocities in the northern Ribeira belt seem to continue down to about 500 km.

[26] Fast *P* and *S* wave anomalies are observed in the upper mantle beneath the western Paraná basin (Figures 9a–9c, 10a–10c, and 11c and 11d).With the exception of the Rio Apa block (a small Proterozoic fragment near station PTMB) these anomalies cannot be directly related to basement rocks because of the sedimentary cover. Beneath the Paraná basin the fast *S* wave anomalies (Figure 10a) may indicate a cratonic nucleus which had been inferred from a few rock samples [*Cordani et al.*, 1994].

[27] In the lower mantle beneath the Paraná basin we observe two regions of high velocities (Figures 9d and 9f, 10d and 10f, and 11a and 11b): one at the west about 500–700 km depth, and another deeper than 1200 km at the center of the study area. These two high-velocity regions could be segments of the subducted lithosphere of the Nazca plate caused by the convergence with the South American plate. We compared our results with the high *P* wave velocity subducted blocks identified by *Engdahl et al.* [1995] just to the west of our region. Figure 12 shows an E-W vertical cross section (profile FF′) combining our *P* wave anomalies in SE Brazil with the high-velocity blocks (blue areas over a yellow background) taken from profile 3f (shown in the study of *Engdahl et al.* [1995, Figures 1 and 3f]). Beneath the Andean region, the high-velocity anomaly between the 410 and 660 km discontinuities was interpreted as "regional emplacement of a recumbent slab" [*Engdahl et al.*, 1995], which explains the occurrence of a deep earthquake beneath Paraguay offset by more than 200 km from the Wadati-Benioff zone. The high-velocity anomaly in the transition zone beneath the Paraná basin strongly suggests the continuation of the recumbent slab further to the east and then possibly plunging to about 1300–1400 km depth. It is not possible to see if the slab is continuous in the transition zone because of lower resolution at the eastern end of Engdahl's profile "3f" and at the western border of our study region. Also, the apparent segmentation between depths of 600–700 and 1300–1400 km in our image may not be real, as will be seen in the resolution tests below.

4. Resolution Analysis

[28] The images we obtained of the mantle beneath SE Brazil display lateral heterogeneities, which can be related to the different geological or tectonic units. However,

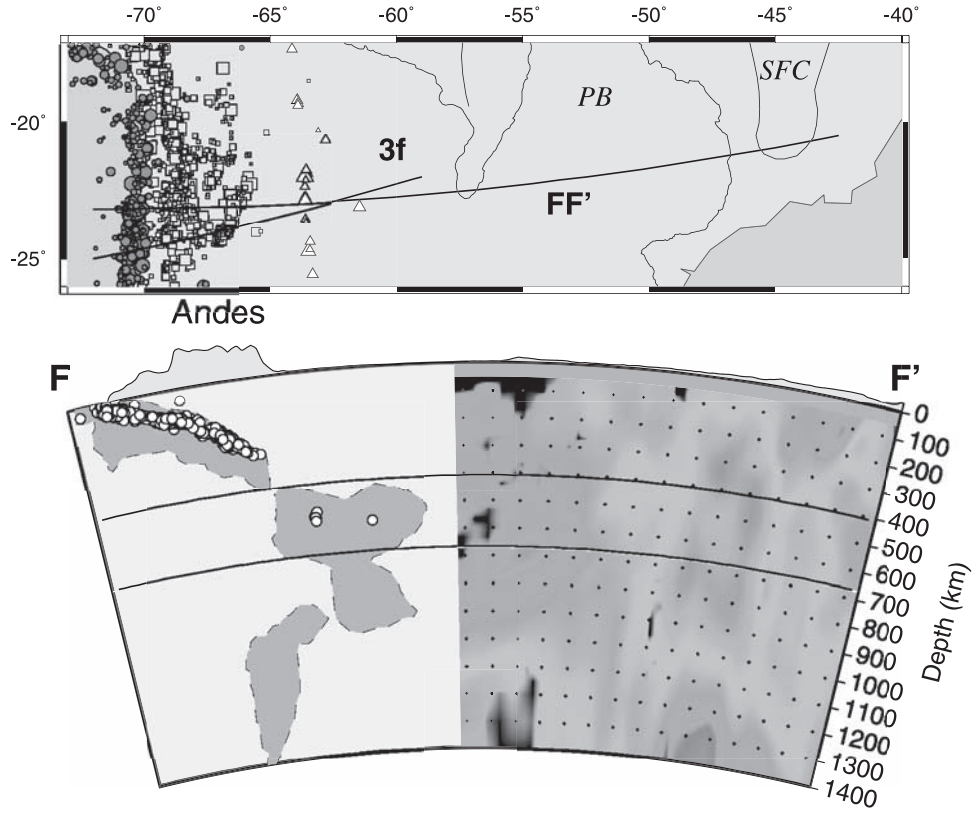

Figure 12. Composite E-W profile of *P* wave anomalies. Top: map showing the location of the profile "3f" of *Engdahl et al.* [1995] and the profile FF′ below. Shallow, intermediate, and deep earthquakes are shown by red circles, yellow squares, and white triangles, respectively (1964–1995 data of *Engdahl et al.* [1998]). PB denotes Paraná basin and SFC denotes São Francisco craton. Bottom: the left-hand side shows the fast-velocity anomalies (blue areas) taken from the profile "3f" of *Engdahl et al.* [1995]. The white circles are hypocenters to within 1° of the line FF′. The right-hand side is our tomography result showing a probable continuation of the flat-lying slab within the transition zone before plunging to greater depths. See text for discussion on the continuity of the slab. See color version of this figure at back of this issue.

without any resolution analysis these images are of little value for interpretation. The unequal distribution of events and stations causes a varying illumination of the target volume (Figure 8) with variable resolution of structure. The visualization and/or calculation of the exact resolution remains a challenge [*Snieder*, 1998; *Trampert*, 1998] owing to the large number of model parameters, errors in the data, and simplifications of the physics of the forward problem. In practice, checker board or special geometry tests are commonly used to display well and badly resolved areas. Here we employ a special geometry test to investigate how well we can recover volumetric heterogeneities with the geometries inferred from the real data images. These results do not represent the true resolution [*Lévêque et al.*, 1993], but give an important insight.

[29] For the first test inversion (Figures 13a, 13c, and 13e) we use an input model with a fast-velocity anomaly simulating a 170 km thick São Francisco craton (C), an upper mantle low-velocity conduit (L) beneath the Paraná basin, and a horizontally constant velocity perturbation (H) between 350 and 500 km depth. We are more interested in the recovery of the overall geometry and shapes than in the recovery of anomaly amplitudes. The event station configuration was chosen from the *P* wave data set and the synthetic travel times were calculated with a 3-D ray tracer. The inversions use the ray paths in a radial symmetric model similar to the inversion of the observed data that are not the 3-D ray paths from the synthetic forward problem. In the inversions, we added Gaussian noise with a standard deviation of 25% of the RMS of the synthetic data residuals. The addition of noise increases the inconsistencies in the data, which affects regions of low resolution in particular. The applied noise level is larger than we expect to have in the real data.

[30] The reconstructed input model is shown in Figures 13b, 13d, and 13f and explains 84% of the RMS data residual. Note the percentage velocity scale has been reduced to show the full range of amplitudes. The recovered model is smooth since strong spatial velocity gradients are reduced through the regularization of the inversion. It is obvious from the figure that the horizontal velocity anomaly layer (H) is not resolved. This is expected since the relative residuals of each event were demeaned. Due to the demeaning we get rid of any source of constant travel time contribution such as errors in the origin time or lateral constant velocity perturbations outside or inside the study

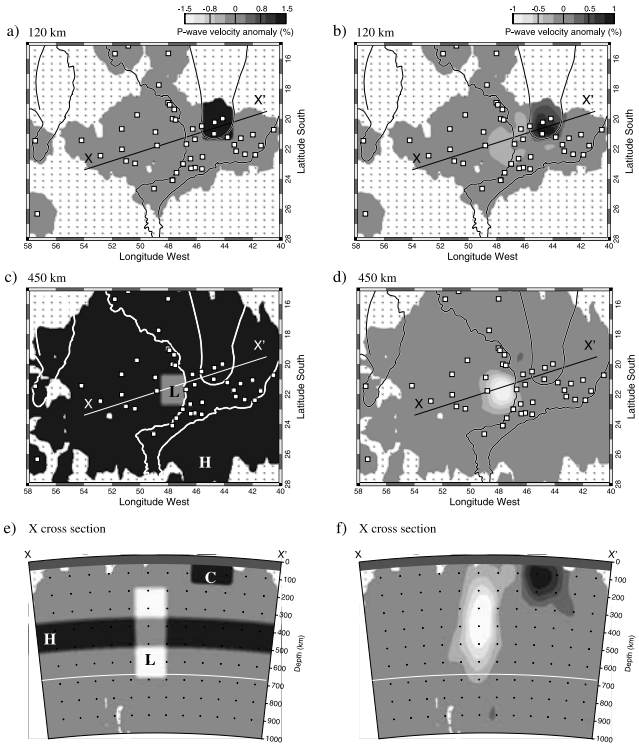

Figure 13. Input model (a, c, and e) with *P* wave velocity anomalies. The fast and slow anomalies are displayed by dark and light gray tones, respectively. Gray dots on white background indicate the areas with low ray density and poor resolution. Travel times for the *P* wave data sets were obtained by 3-D ray tracing and contaminated by Gaussian noise with standard deviation of 25% of the synthetic data RMS residual. The corresponding reconstructions are shown in b, d, and f.

volume. Thus removing the mean from each earthquake data prevents the detection of constant velocity layers. Our tomographic approach reconstructs only horizontal velocity contrasts. This has to be taken into account when interpreting the resulting anomaly model.

[31] The low-velocity conduit (L) is resolved but vertically elongated. The elongation is larger at its top than at its base because of the steeper ray paths and decreasing number of crossing rays at shallow depth. For the same reason, the São Francisco craton (C) is better resolved laterally than vertically.

[32] In the following we test a more complicated input model (Figure 14). The *S* wave velocity anomalies simulate two slab segments (S1 and S2), a N-S elongated low-velocity anomaly in the lower mantle (L2), two high-velocity cratonic roots (C1 and C2), a cylindrical low-velocity conduit (L1), and another high-velocity anomaly in the upper mantle (H1). The event station configuration was chosen from the *S* wave data set, which has a better ray coverage at larger depth (Figure 8), and the synthetic travel times were contaminated with 25% Gaussian noise.

[33] The reconstructed input model is displayed in Figure 15 and explains 87% of the RMS of the synthetic data residuals. From Figure 15 it can be seen that the upper mantle low-velocity anomaly (L1) in the center of the study volume is well resolved. The elongation at the base reaches about 100 km. Also, the São Francisco craton (C2) is well constrained laterally and can even be separated from a high-velocity anomaly (H1) to the east (Figures 15a, 15b, and 15e). A hypothesized cratonic nucleus in the Paraná basin (C1) cannot be isolated from a slab segment (S1) at the top of the lower mantle (Figure 15e). The blurred images demonstrate the poor vertical resolution in this portion of the target volume. Below 700 km, we obtain better lateral than vertical resolution. This is mainly caused by the finite size of the array aperture, which limits the range of crossing ray angles. The generally steep rays give rise to the vertical blur of anomalies.

[34] A third input model (Figure 16) was designed to test whether we should be able to resolve a continuous high-velocity slab and low-velocity conduit. The model contains a hypothetical São Francisco craton (C) with roots down to 200 km. For the inversion we use *S* wave data with 25% Gaussian noise contamination. The reconstructions shown in Figure 17 explain 87% of the RMS data residual. From Figure 17 it is seen that a continuous slab is imaged as two separated slab segments. Thus, we cannot resolve whether there are separated or continuous slab segments in the lower mantle. This cannot be attributed to the demeaning of the residuals since the inversion of the nondemeaned synthetic residuals yields similar results. Also, the patchy images of the slab in the horizontal depth sections (Figures 15c and 15d and 17c and 17d) remain for the inversions of nondemeaned residuals. Although we cannot see whether the

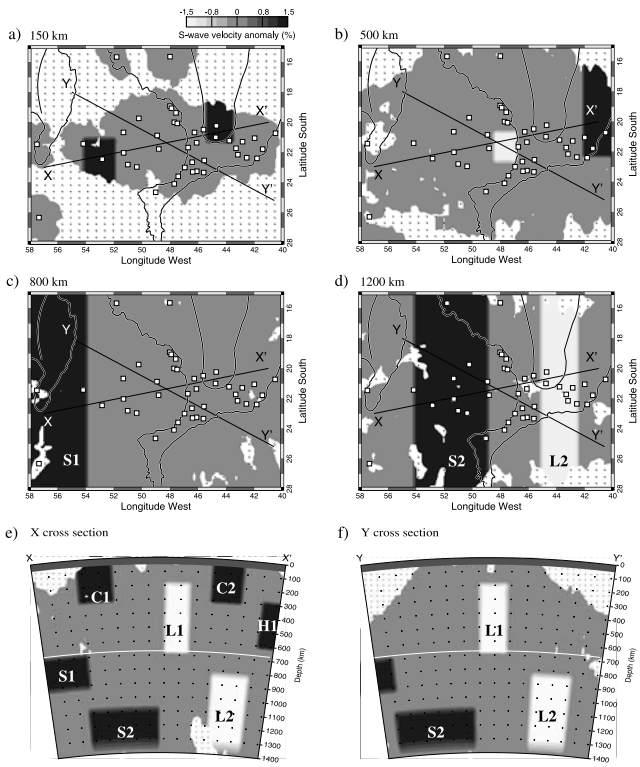

Figure 14. Input model with *S* wave velocity anomalies used for the resolution test inversions. The fast and slow anomalies are displayed by dark and light gray tones, respectively. Gray dots on white background indicate the areas with low ray density.

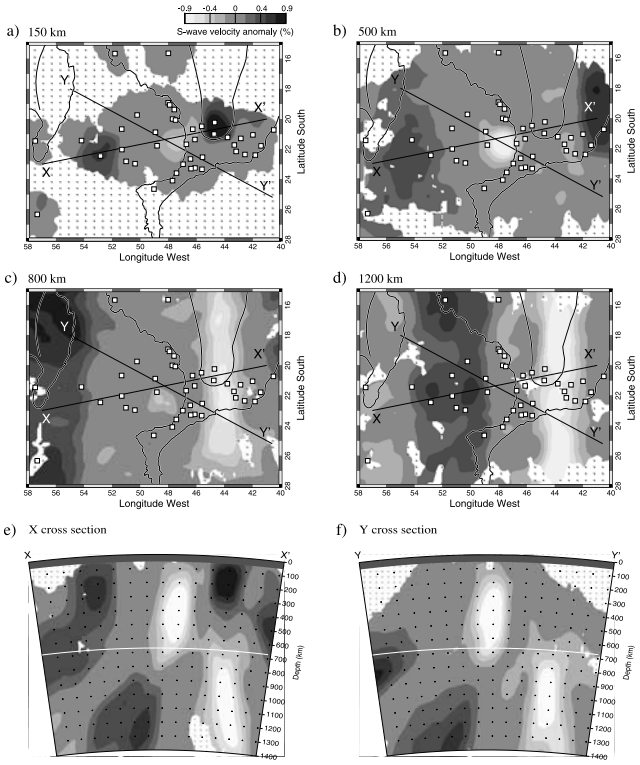

Figure 15. Reconstructed model. The event station configuration is from the *S* wave data set. Travel times were obtained by 3-D ray tracing and contaminated by Gaussian noise with standard deviation of 25% of the synthetic data RMS residual.

slab is segmented or continuous we can conclude that parts of the subducted Nazca plate are visible in our true data images because of the N-S pattern. We do not refrain from showing the images down to the less resolved depth to improve the overall understanding of the reconstructions. Figures 15 and 17 show that we should be able to distinguish between a continuous or isolated low-velocity conduit in the real data inversions. Also, the hypothetical São Francisco craton with different depth extension has different responses in the corresponding reconstructions. From comparisons with the test inversions, we expect that the São Francisco craton has roots to about 200–250 km depth.

[35] Besides the synthetic data inversions and true data inversions on subsidiary data sets we computed velocity anomaly models where structure is allowed in the upper 400 km only. A reconstruction which explains 83% of the RMS data residual is shown in Figure 18. From a comparison with Figures 9a and 9b it can be seen that the large-scale features are the same. The differences occur in the low-resolution areas such as beneath the western Paraná basin and east of the São Francisco craton. These small differences are not unexpected since the inversion tries to map structure from outside the study volume into the less constrained low-resolution areas. Similar effects happen in simulations where we invert the synthetic data from Figure 14 for structure in the uppermost 400 km only. The larger study volume contains other poorly resolved areas that can act as buffer for data inconsistencies preventing contamination of the better resolved areas. Our interpretation of the images is restricted to the robust gross structure, which we also obtain in the reconstructions for the different subsidiary data sets or regularizations.

5. Discussion

[36] The independently inverted *P* and *S* wave relative residuals consistently show the presence of a cylindrical low-velocity anomaly in the well-resolved center of the study area. Its interpretation as a fossil conduit of the initial Tristan da Cunha plume head [*VanDecar et al.*, 1995] implies that the upper mantle has been in coupled motion with the overlying plate to explain the persistence of the anomaly below the Paraná basin. The base of the anomaly had not been imaged until now and the increased aperture of the seismic array and the higher data density enabled us to show that this structure is mostly confined to the upper mantle. From the *P* wave images, however, it seems that this anomaly could be continuous down to about 800–900 km. We believe that this can be an artifact due to the vertical elongation of the anomaly since there are less crossing rays (Figures 8a and 8c) at the top of the lower mantle in the *P* wave data set. Besides, one must keep in mind that we resolve only lateral velocity anomalies. The absolute velocities are unknown and the images depend on the reference model (IASP91 in our case). The cylindrical anomaly changes to a N-S horizontally oriented anomaly around 500–600 km (Figures 9c and 9d and 10c and 10d); this N-S low-velocity anomaly probably enters into the upper most

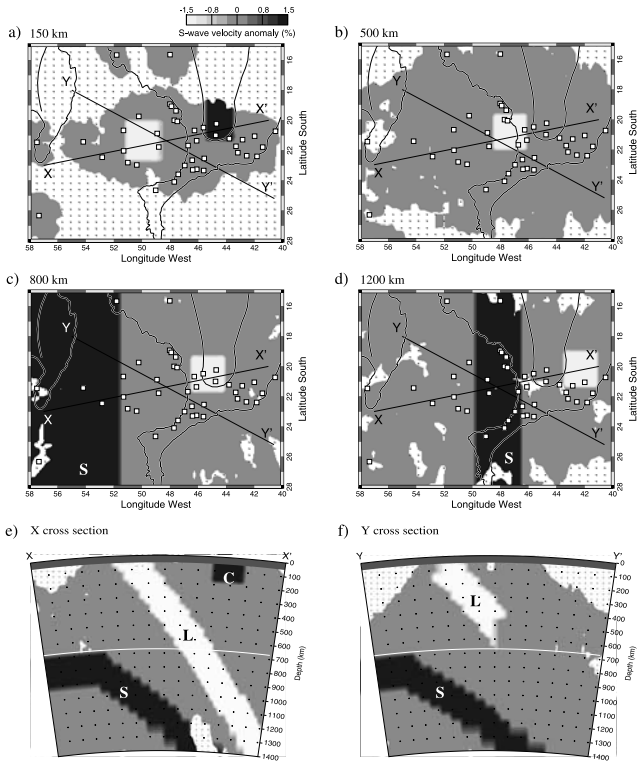

Figure 16. Input model with *S* wave velocity anomalies used for the resolution test inversions. The fast and slow anomalies are displayed by dark and light gray tones, respectively. Gray dots on white background indicate the areas with low ray density.

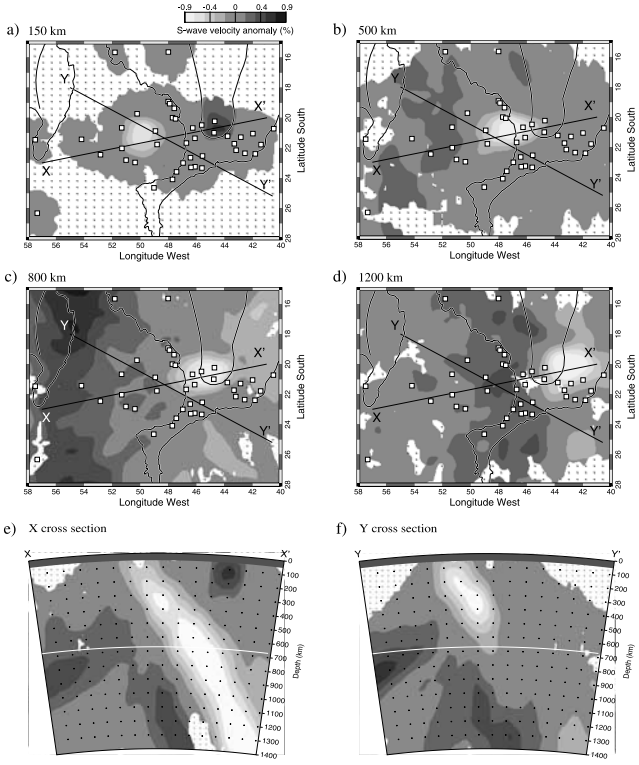

Figure 17. Reconstructed model. The event station configuration is from the *S* wave data set. Travel times were obtained by 3-D ray tracing and contaminated by Gaussian noise with standard deviation of 25% of the synthetic data RMS residual.

part of the lower mantle (down to about 800 km, Figure 11). Because our inversion only detects lateral velocity contrasts, the N-S oriented low-velocity anomaly can be just a result of the lateral contrast with a high-velocity slab to the west. A decrease of the reference *P* wave velocities at 700–900 km would increase the high-velocity anomalies and decrease the low-velocity anomalies. At the top of the lower mantle, this would mean a stronger slab and a weaker low-velocity anomaly. The presence of the cylindrical low-velocity anomaly at about 300 km depth is confirmed by a higher mode surface wave study by *Van der Lee et al.* [2001]. Our results do not indicate the continuation of the cylindrical low-velocity anomaly into the lower mantle.

[37] At roughly 1300 km depth another N-S elongated low-velocity structure appears parallel to the slab. These large-scale anomalies at the base of our study volume are not well resolved, blurred into shallower depths, and imaged as patchy pattern as also visible in our synthetic test inversion results. Our test inversions only show that if the structure we interpret is real then we would see it such as imaged in the real data inversions. These inversions confirm that separate anomalies such as L1 and L2 (Figure 15) can be identified by the employed data configuration although the images are slightly vertically elongated. Further, from Figure 17 it is not expected that a continuous low-velocity conduit is imaged as separate units. We therefore believe that the upper mantle anomaly is not connected to the other deeper, low-velocity anomaly. The similarity of *P* and *S* wave inversions strengthens the credibility of this isolation.

[38] The existence of low-velocity anomalies near each alkaline province (Figures 9a and 10a) in the fold belts can indicate their origin/trigger by an upper mantle heat source. *Gibson et al.* [1999] found geochemical evidence indicating that most of the volume of the alkaline rocks originate from the subcontinental lithosphere which is consistent with the generally low velocities associated with the alkaline provinces at lithospheric depths in our models. The origin of these Late Cretaceous alkaline intrusions is still controversial. The fossil plume model of *VanDecar et al.* [1995] suggests that these postrift intrusions were somehow a late effect of the previous Tristan da Cunha plume. *Gibson et al.* [1999] prefer to associate the Late Cretaceous intrusions to the Trindade plume whose track runs about 1000 km north of the Tristan da Cunha track (see Figure 1). Recent Ar-Ar age determinations for the alignment of intrusions in the central part of the Ribeira belt (roughly at 22°–23°S) led *Szatmari et al.* [2000] to postulate a third, independent hot spot track. We hope that the correlation of velocity anoma-

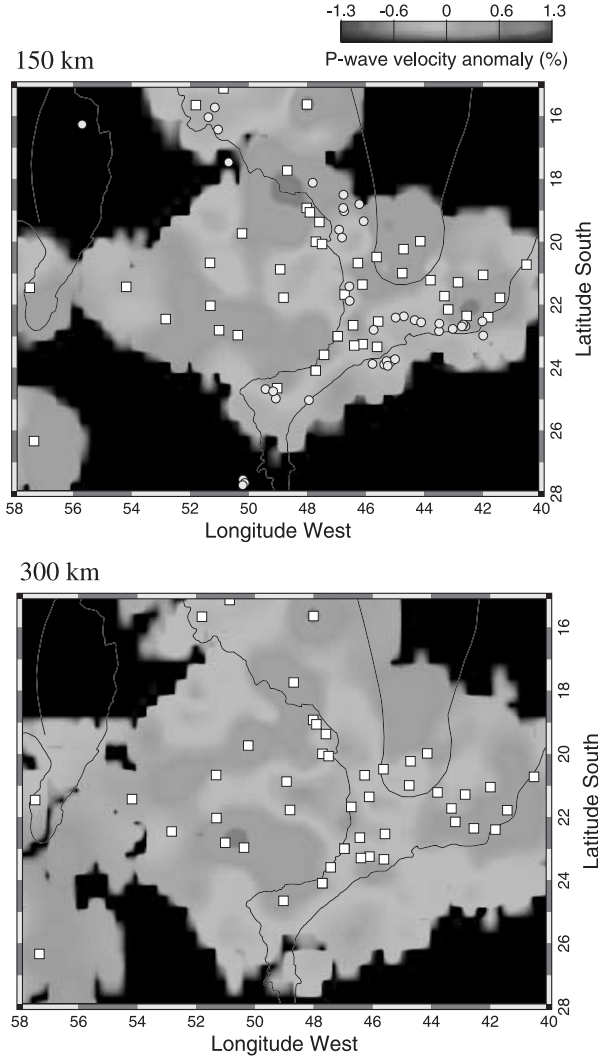

Figure 18. *P* wave velocity anomalies obtained in a test inversion for structure down to 400 km only. White squares and yellow circles (a) denote station sites and Late Cretaceous alkaline intrusions, respectively. See color version of this figure at back of this issue.

lies at lithospheric depths with the alkaline provinces may help better understand their origin.

[39] The much older and colder São Francisco craton is visible as high-velocity *P* and *S* wave anomaly with roots down to depth of 200 and 300 km, respectively. On the basis of the vertical blur observed in our tests we believe that the roots of the craton are not deeper than 200–250 km. The observed cratonic keel indicates that the craton is a strong and stable feature, not much perturbed thermally, in concordance with its low heat flow [*Vitorello et al.*, 1980]. Besides the thermal perturbations the craton resisted the collision with the Congo craton during the consolidation of western Gondwana in the Brasiliano orogenic cycle with formation of the surrounding Ribeira fold belts and highest stresses at the southern termination of the craton [*Vauchez et al.*, 1994].

[40] The shallow part of a fast-velocity anomaly to the east of the craton could be related to a geological complex with rocks of late Archean age, reworked during the Brasiliano cycle [*Schobbenhaus*, 1984]. However, it seems that this anomaly extends down to the base of the upper mantle, which cannot be related to the exposed geological units. This *P* and *S* wave anomaly at the base of the upper mantle can be real, but its shape and position is not well constrained. High velocities in this area (from the northern Ribeira belt to the east) can also be observed in the Rayleigh and Love wave maps at 100–150 s periods by *Vdovin et al.* [1999]. Fundamental surface waves at these periods are dominantly sensitive to the *S* velocities between 100 and 200 km depth and therefore sample only the upper part of the anomaly. High upper mantle velocities beneath the transition from thick continental lithosphere to thin oceanic lithosphere have been observed in eastern South America by *King and Ritsema* [2000] and explained as due to edge-driven convection with downwellings extending to the base of the upper mantle. The observed high velocities beneath the northern Ribeira belt are consistent with this explanation.

[41] Mainly from the *S* velocity perturbation models, a cratonic nucleus can be inferred for the Paraná basin east of the Rio Apa block (Figures 10a and 9a). Such a nucleus has been suggested by *Cordani et al.* [1994] and *Brito Neves et al.* [1984] based on the ages of drill cores from northern Paraná, and on the organization of the surrounding mobile belts. The drill cores from 3.5 km depth yield Proterozoic ages of about 2.1 Ga. Due to the presence of sedimentary cover rocks and CFB there is no surface evidence for a cratonic nucleus. The observed high *S* wave velocities confirm the cratonic lithosphere structure. Surface wave dispersion studies [*Snoke and James*, 1997; *Assumpção et al.*, 2002] indicate high upper mantle velocities (4.6–4.7 km/s) for the average Paraná basin down to about 100 km, comparable to the São Francisco craton. A direct comparison between surface wave studies and our tomographic results is not possible due to the different resolutions. Our synthetic tests show a poor depth resolution that permits no separation between a high-velocity anomaly from the top of the lower mantle and the roots of a hypothesized craton in the Paraná basin (Figure 15e). Surprisingly, the *P* velocity perturbation model show only a weak signature which could be due to the inversion parameters and settings, to the low resolution, or to a varying Poisson ratio. Only the Rio Apa block appears as fast-velocity anomaly for the *P* and *S* waves in the shallow structure of the west Paraná basin.

[42] The slab-shaped anomalies in the lower mantle can be recognized as part of the circum-Pacific patterns found in various studies and which are connected with past subduction [e.g., *Grand*, 1994; *Van der Hilst et al.*, 1997; *Bijwaard et al.*, 1998]. Beneath SE Brazil, we observe the subducted lithosphere of the Nazca plate caused by the convergence with the South American plate. For SE Brazil, the resolution of the global studies is poor due to a small data coverage. *Grand* [1994] [see also *Van der Hilst et al.*, 1997, Figure 3] traces signatures of the slab down to about 1350 km. At depth of 810 km, the slab is also visible in the images by *Bijwaard et al.* [1998]. Their positions coincide with our reconstructions. The slab at about 500–700 km depth (Figures 9d–9f, 10d–10f, 11, and 12) may belong to a partly deflected and recumbent portion in the upper mantle transition zone [*Engdahl et al.*, 1995]. A second slab segment is observed in the lower mantle at about 1300–1400 km depth. The test computations showed that a lower mantle slab is not uniformly resolved and that we cannot therefore constrain whether there are two slab segments or one continuous slab segment.

6. Conclusions

[43] The increased aperture of the seismic network and the high data density permitted us to image, with improved resolution, the seismic velocity anomalies in an enlarged volume of mantle underneath SE Brazil. The largest part of this study volume has been mapped for the first time on a regional scale. Most large-scale anomalies are consistently observed in our independent *P* and *S* wave inversion solutions and remain as robust features in the different inversion results. The test inversions of synthetic data indicate that the resolution is sufficient to support the interpretations of the large-scale features in our images. The most prominent anomalies of the upper mantle are the São Francisco craton, which is visible as fast-velocity perturbation with roots down to 200–250 km depth, and an isolated low-velocity anomaly beneath the Paraná basin. The cratonic root is considered as evidence for a strong and stable craton, since it survived the thermal and geodynamical events of the past. Similarly, we can conclude that the Varginha-Guaxupe complex is a stable block seismically visible down to about 200 km depth. The low-velocity anomaly beneath the Paraná basin has been interpreted as the fossil conduit of the initial Tristan da Cunha plume head. The interpretation of this anomaly and its persistence underneath the Paraná basin implies that the upper mantle and overlying South American plate moved as one unit at least since the opening of the South Atlantic. Besides, it is seen that the fold belts and most of the exposed Late Cretaceous alkaline intrusions are correlated to lower than average mantle velocities around 200 km depth. This suggests that the alkaline intrusions have their origin in the uppermost mantle. A high *S* wave velocity anomaly in the middle of the Paraná basin is consistent with the earlier proposed cratonic lithosphere structure. The origin of the fast upper mantle anomaly to the east of the São Francisco craton is not yet clear. The most striking features of the lower mantle are the partly imaged subducted Nazca Plate and the low-velocity anomalies parallel to the slabs. The shape and position of these anomalies are not well constrained. Never-

theless these anomalies are expected and one may conclude that, in spite its limitation, regional inversion of relative residual times can detect large-scale anomalies below the upper mantle.

[44] **Acknowledgments.** The data are from GTSN, GEOSCOPE, UnB, RESUSP, and BLSP stations and we are very grateful to all the researchers and technicians who somehow contributed to these data. M.S. likes to thank Andrea Tommasi and Alain Vauchez for valuable discussions and the seismology group from the Carnegie Institution and the tectonophysics group from Montpellier for their hospitality during a visit. The constructive reviews by the associate editor Rob Van der Hilst, the referee Ray Russo, and an anonymous referee improved the manuscript. With exception of the tomographic images, plots were done using Seismic Analysis Code (SAC), provided by Lawrence Livermore National Laboratory of the University of California, and Generic Mapping Tools (GMT) by *Wessel and Smith* [1991]. This work is supported by Fundação de Amparo à Pesquisa do Estado de São Paulo (FAPESP) grants 97/03640-6 and 97/04780-6 and CNPq grant 30.0227/79.

References

Assumpção, M., D. James, and J. A. Snoke, Crustal thickness in SE Brazilian shield by receiver function analysis: Implications for isostatic compensation, *J. Geophys. Res.*, *107*(B1), 2006, doi:10.1029/2001JB000422, 2002.

Bijwaard, H., W. Spakman, and E. R. Engdahl, Closing the gap between regional and global travel time tomography, *J. Geophys. Res.*, *103*, 30,055–30,078, 1998.

Brito Neves, B. B., and U. G. Cordani, Tectonic evolution of South America during the Late Proterozoic, *Precambrian Res.*, *53*, 23–40, 1991.

Brito Neves, B. B., R. Fuck, U. G. Cordani, and A. Thomaz, Influence of basement structures on the evolution of the major sedimentary basins of Brazil: A case of tectonic heritage, *J. Geodyn.*, *1*, 495–510, 1984.

Cline, A. K., *FITPACK-Software Package for Curve and Surface Fitting Employing Splines Under Tensions*, Dept. of Comput. Sci., Univ. of Tex. at Austin, Austin, Tex., 1981.

Constable, S. C., R. L. Parker, and C. G. Constable, Occams inversion: A practical algorithm for generating smooth models from electromagnetic sounding data, *Geophysics*, *52*, 289–300, 1987.

Cordani, U. G., B. B. Brito Neves, R. A. Fuck, R. Porto, A. T. Filho, and F. M. Bezerra da Cunha, Estudo preliminar de integração do Pré-cambriano com os eventos tectônicos das bacias sedimentares brasileiras, in *Revista Cienca Tecnica Petroleo, Rep. 15*, 70 pp., Petrobrás, Cent. de Pesqui. e Desenvolvimento Leopoldo A. Maguez de Mello (CENPES), Rio de Janeiro, Brazil, 1994.

Engdahl, E. R., R. D. Van der Hilst, and J. Berrocal, Imaging of subducted lithosphere beneath South America, *Geophys. Res. Lett.*, *22*, 2317–2320, 1995.

Engdahl, E. R., R. D. Van der Hilst, and R. P. Buland, Global teleseismic earthquake relocation with improved travel times and procedures for depth determination, *Bull. Seismol. Soc. Am.*, *88*, 722–743, 1998.

Gibson, S. A., R. N. Thompson, O. H. Leonardos, A. P. Dickin, and J. G. Mitchell, The limited extent of plume–lithosphere interactions during continental flood-basalt genesis: Geochemical evidence from Cretaceous magmatism in southern Brazil, *Contrib. Mineral. Petrol.*, *137*, 147–169, 1999.

Grand, S. P., Mantle shear structure beneath the Americas and surrounding oceans, *J. Geophys. Res.*, *99*, 11,591–11,621, 1994.

Huber, P. J., *Robust Statistics*, John Wiley, New York, 1981.

James, D. E., and M. Assumpção, Tectonic implications of *S*-wave anisotropy beneath SE Brazil, *Geophys. J. Int.*, *126*, 1–10, 1996.

Kennett, B. L. N., and E. R. Engdahl, Travel times for global earthquake location and phase identification, *Geophys. J. Int.*, *105*, 429–465, 1991.

Kennett, B. L. N., and S. Widiyantoro, A low seismic wavespeed anomaly beneath northwestern India: A seismic signature of the Deccan plume?, *Earth Planet Sci. Lett.*, *165*, 145–155, 1999.

King, S. D., and J. Ritsema, African hot spot volcanism: Small-scale convection in the upper mantle beneath cratons, *Science*, *290*, 1137–1140, 2000.

Lévêque, J.-L., L. Rivera, and G. Wittlinger, On the use of the checkerboard test to assess the resolution of tomographic inversions, *Geophys. J. Int.*, *115*, 313–318, 1993.

Neele, F., J. VanDecar, and R. Snieder, The use of P-wave amplitude data in a joint inversion with travel times for upper mantle velocity structure, *J. Geophys. Res.*, *98*, 12,033–12,054, 1993.

O'Connor, J. M., and R. A. Duncan, Evolution of the Walvis Ridge-Rio Grande Rise hot spot system: Implications for African and South American plate motions over plumes, *J. Geophys. Res.*, *95*, 17,475–17,502, 1990.

Paige, C. C., and M. A. Saunders, LSQR: An algorithm for sparse linear equations and sparse least squares, *ACM Trans. Math. Software*, *8*, 43–71, 1982.

Peate, D. W., C. J. Hawkesworth, M. M. S. Mantovani, N. W. Rodgers, and S. P. Turner, Petrogenesis and stratigraphy of the high Ti/Y Urubici magma type in the Paraná flood basalt province and implications for the nature of "Dupal"-type mantle in the South Atlantic region, *J. Petrol.*, *40*, 451–473, 1999.

Pulliam, R. J., D. W. Vasco, and L. R. Johnson, Tomographic inversions for mantle P wave velocity structure based on the minimization of l^2 and l^1 norms of International Seismological Centre travel time residuals, *J. Geophys. Res.*, *98*, 699–734, 1993.

Renne, P. R., K. Deckart, M. Ernesto, G. Féraud, and E. M. Piccirillo, Age of Ponta Grossa dike swarm (Brazil), and implications to Paraná flood volcanism, *Earth Planet Sci. Lett.*, *144*, 199–211, 1996.

Richardson, W. P., E. A. Okal, and S. Van der Lee, Rayleigh-wave tomography of the Ontong-Java Plateau, *Phys. Earth Planet Inter.*, *118*, 29–51, 2000.

Ritsema, J., A. A. Nyblade, T. J. Owens, C. A. Langston, and J. C. VanDecar, Upper mantle seismic velocity structures beneath Tanzania, east Africa: Implications for the stability of cratonic lithosphere, *J. Geophys. Res.*, *103*, 21,201–21,213, 1998.

Schimmel, M., Phase cross-correlations: design, comparisons and applications, *Bull. Seismol. Soc. Am.*, *89*, 1366–1378, 1999.

Schobbenhaus, C., *Geologic Map of Brazil and Adjoining Ocean Floor Including Mineral Deposits*, Editora S.A. Abril, São Paulo, 1984.

Silveira, G., E. Stutzmann, D.-A. Griot, J.-P. Montagner, and L. M. Victor, Anisotropic tomography of the Atlantic Ocean from Rayleigh surface waves, *Phys. Earth Planet Inter.*, *106*, 257–273, 1998.

Snieder, R., The role of nonlinearity in inverse problems, *Inverse Probl.*, *14*, 387–404, 1998.

Snoke, J. A., and D. E. James, Lithospheric structure of the Chaco and Paraná Basins of South America from surface-wave inversion, *J. Geophys. Res.*, *102*, 2939–2951, 1997.

Sobolev, S. V., A. Grésillaud, and M. Cara, How robust is isotropic delay time tomography for anisotropic mantle?, *Geophys. Res. Lett.*, *26*, 509–512, 1999.

Szatmari, P., J. Conceicao, N. Destro, P. Smith, N. Evensen, and D. York, Tectonic and sedimentary effects of a hot-spot track of alkali intrusions defined by Ar-Ar dating in SE Brazil, *31th Geological Congress, Abstracts Volume (CD-ROM)*, Rio de Janeiro, 2000.

Trampert, J., Global seismic tomography: the inverse problem and beyond, *Inverse Probl.*, *14*, 371–385, 1998.

Trompette, R., *Geology of Western Gondwana* (*2000–500 Ma*), *Pan-African–Brasiliano Aggregation of South America and Africa*, A. A. Balkema, Brookfield, Vt., 1994.

VanDecar, J. C., and R. S. Crosson, Determination of teleseismic relative phase arrival times using multi-channel cross-correlation and least squares, *Bull. Seismol. Soc. Am.*, *80*, 150–169, 1990.

VanDecar, J. C., D. E. James, and M. Assumpção, Seismic evidence for a fossil plume beneath South America and implications for plate driving forces, *Nature*, *378*, 25–31, 1995.

Van der Hilst, R. D., S. Widiyantoro, and E. R. Engdahl, Evidence for deep mantle circulation from global tomography, *Nature*, *386*, 578–584, 1997.

Van der Lee, S., D. James, and P. Silver, Upper mantle *S*-velocity structure of central and western South America, *J. Geophys. Res.*, *106*, 30,821–30,834, 2001.

Vauchez, A., A. Tommasi, and Egydio-Silva, Self-indentation of a heterogeneous continental lithosphere, *Geology*, *22*, 967–970, 1994.

Vauchez, A., G. Barruol, and A. Tommasi, Why do continents break up parallel to ancient orogenic belts?, *Terra Nova*, *9*, 62–66, 1997.

Vdovin, O., J. A. Rial, A. L. Levshin, and M. H. Ritzwoller, Group-velocity tomography of South America and the surrounding oceans, *Geophys. J. Int.*, *136*, 324–340, 1999.

Vitorello, I., V. M. Hamza, and H. Pollack, Terrestrial heat flow in the Brazil highlands, *J. Geophys. Res.*, *85*, 3778–3788, 1980.

Wessel, P., and W. H. F. Smith, Free software helps map and display data, *Eos Trans. AGU*, vol. 72, p. 441, 445–446, 1991.

Wolfe, C. J., I. T. Bjarnason, J. C. VanDecar, and S. C. Solomon, Seismic structure of the Iceland mantle plume, *Nature*, *385*, 245–247, 1997.

M. Assumpção, Department of Geophysics, University of São Paulo, Rua do Matão 1226, 05508-900, São Paulo, Brazil. (marcelo@iag.usp.br)

M. Schimmel, Institute of Earth Sciences "Jaume Almera", Consejo Superior de Investigaciones Cientificas (CSIC), c/ Lluis Sole i Sabaris s/n, 08028, Barcelona, Spain. (schimmel@ija.csic.es)

J. C. VanDecar, Carnegie Institution of Washington, 5241 Broad Branch Road, NW, Washington, DC 20015, USA.

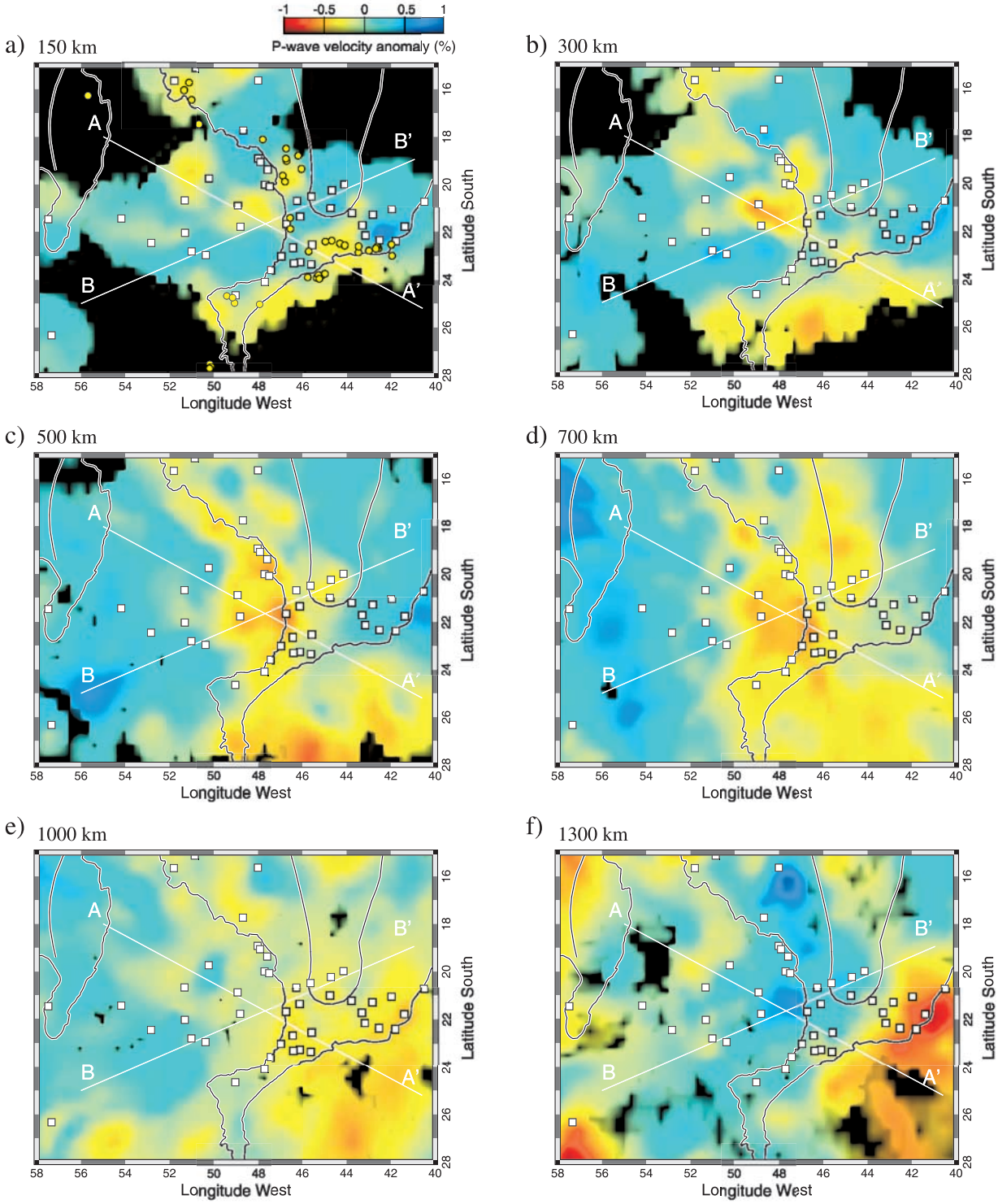

Figure 9. Tomographic reconstructions for the *P* wave phase times at distinct depth levels. White lines mark the intersections with the vertical cross sections (A-A′ and B-B′) displayed in Figure 11. White squares and yellow circles (a) denote station sites and Late Cretaceous alkaline intrusions (ages range from 90 to 55 Ma), respectively.

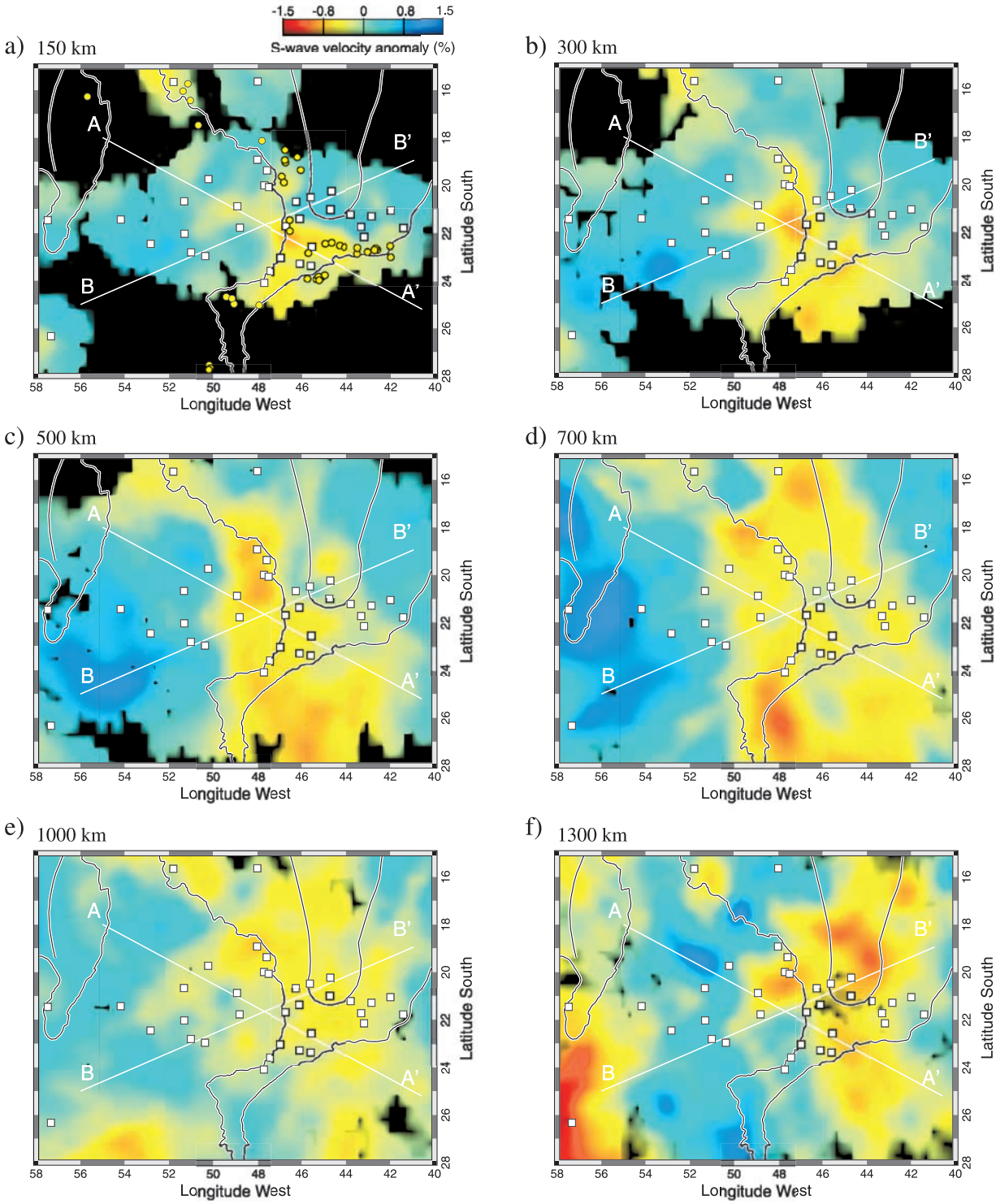

Figure 10. Tomographic reconstructions for the *S* wave phase times at distinct depth levels. White lines mark the intersections with the vertical cross sections (A-A′ and B-B′) that are displayed in Figure 11. White squares denote station sites used in the *S* wave inversion. The yellow circles (a) denote Late Cretaceous alkaline intrusions (ages range from 90 to 55 Ma).

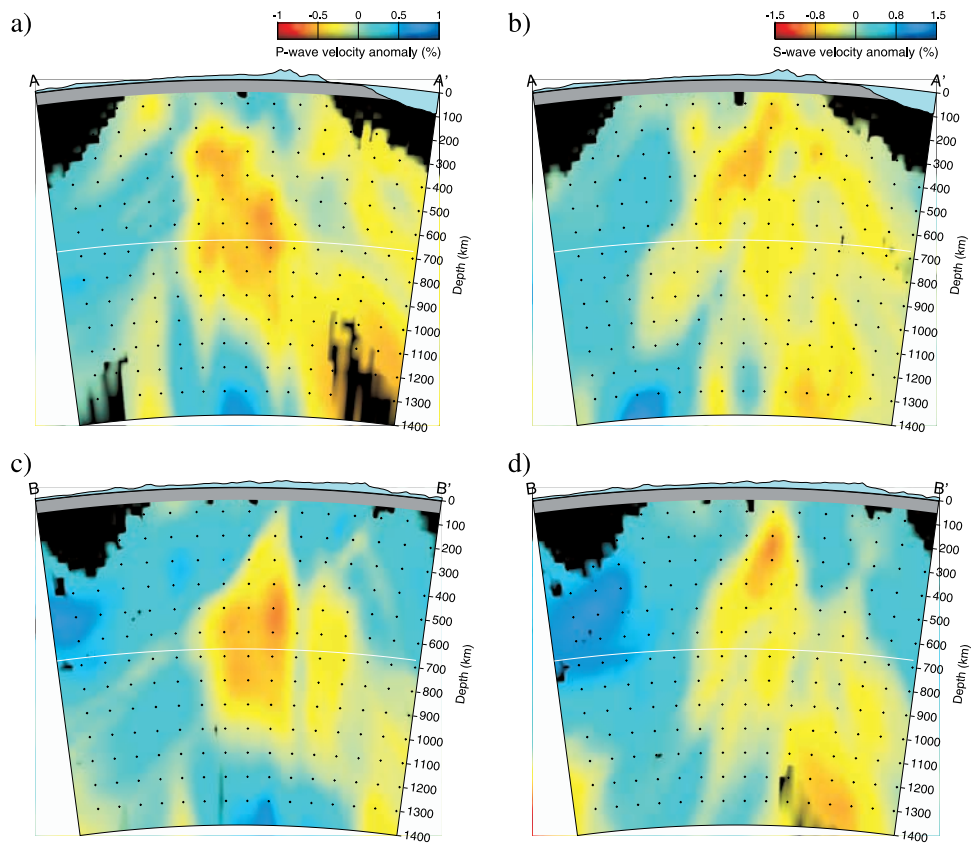

Figure 11. The vertical cross sections A-A′ and B-B′ are displayed for the *P* (left column) and *S* (right column) velocity perturbation models. The elevations at the Earth's surface are multiplied by 30.

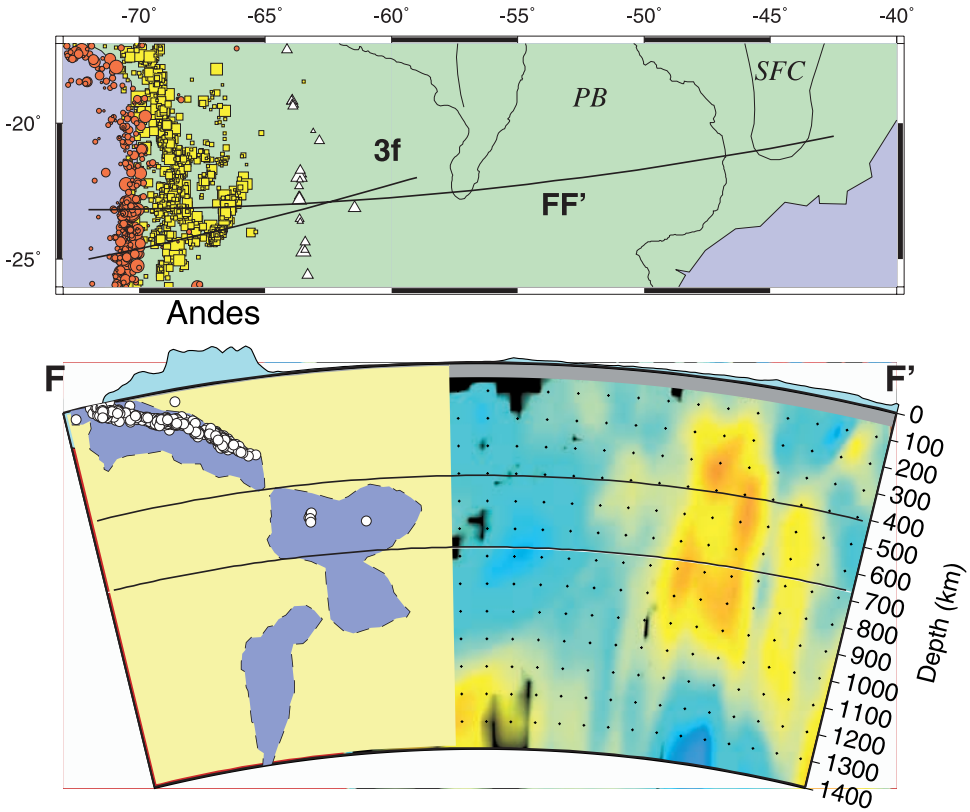

Figure 12. Composite E-W profile of *P* wave anomalies. Top: map showing the location of the profile "3f" of *Engdahl et al.* [1995] and the profile FF′ below. Shallow, intermediate, and deep earthquakes are shown by red circles, yellow squares, and white triangles, respectively (1964–1995 data of *Engdahl et al.* [1998]). PB denotes Paraná basin and SFC denotes São Francisco craton. Bottom: the left-hand side shows the fast-velocity anomalies (blue areas) taken from the profile "3f" of *Engdahl et al.* [1995]. The white circles are hypocenters to within 1° of the line FF′. The right-hand side is our tomography result showing a probable continuation of the flat-lying slab within the transition zone before plunging to greater depths. See text for discussion on the continuity of the slab.

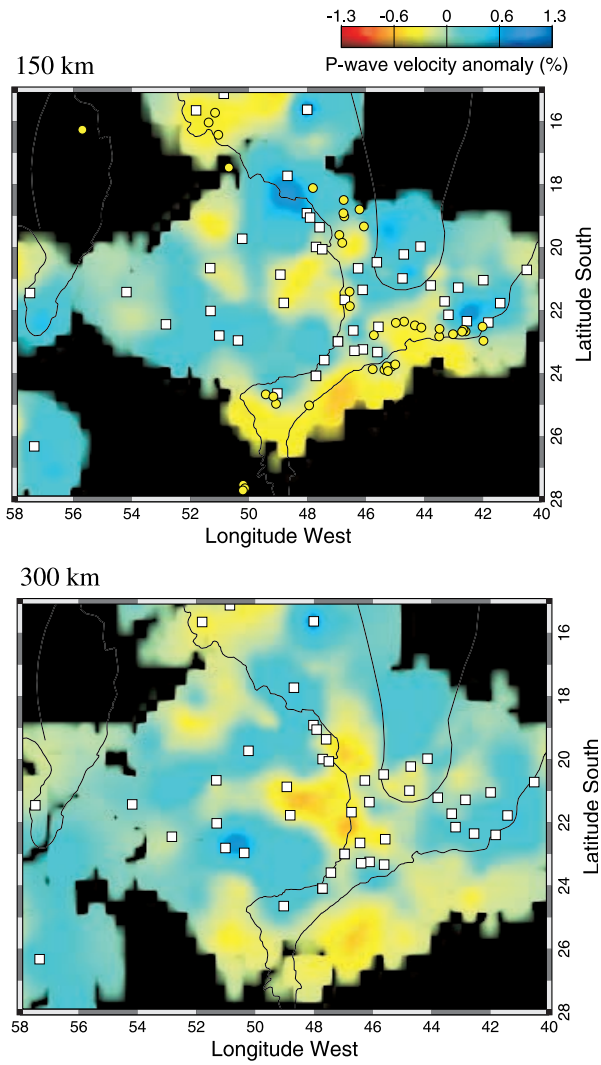

Figure 18. *P* wave velocity anomalies obtained in a test inversion for structure down to 400 km only. White squares and yellow circles (a) denote station sites and Late Cretaceous alkaline intrusions, respectively.